exposure to elevated combustion temperatures and flames.

The fabrication of soft robots using multimaterial 3D printing has numerous advantages over traditional molding techniques. This strategy promotes high-throughput prototyping by enabling rapid design iteration with no additional cost for increased morphological complexity. By allowing designers greater freedom, 3D printing also facilitates the implementation of good robotic design principles, such as modularity and the separation of power and control actuators. Beyond soft robotics specifically, the ability to print a single structure composed of multiple materials enables investigation into mechanically complex designs, without the drawbacks of complicated assembly or inconsistent manufacturing repeatability. One such design is a modulus gradient that eases the transition from soft to rigid components through stress reduction at the interface of materials mismatched in compliance. Although the materials available to this fabrication strategy are currently limited and perhaps best suited to the fabrication of prototype devices, future development of materials compatible with 3D printing will only enhance the relevance of this approach.

REFERENCES AND NOTES

1. D. Rus, M. T. Tolley, *Nature* **521**, 467–475 (2015).
2. D. Trivedi, C. D. Rahn, W. M. Kier, I. D. Walker, *Appl. Bionics Biomech.* **5**, 99–117 (2008).
3. R. Pfeifer, M. Lungarella, F. Iida, *Commun. ACM* **55**, 76 (2012).
4. S. Kim, C. Laschi, B. Trimmer, *Trends Biotechnol.* **31**, 287–294 (2013).
5. C. Majidi, *Soft Robotics* **1**, 5–11 (2014).
6. C. Laschi, M. Cianchetti, *Front. Bioeng. Biotechnol.* **2**, 1–5 (2014).
7. W. McMahan *et al.*, in *Proceedings of the 2006 IEEE International Conference on Robotics and Automation*, 15 to 18 May 2006, Orlando, FL, pp. 2336–2341.
8. R. F. Shepherd *et al.*, *Proc. Natl. Acad. Sci. U.S.A.* **108**, 20400–20403 (2011).
9. C. Laschi *et al.*, *Adv. Robot.* **26**, 709–727 (2012).
10. H.-T. Lin, G. G. Leisk, B. Trimmer, *Bioinspir. Biomim.* **6**, 026007 (2011).
11. C. D. Onal, D. Rus, *Bioinspir. Biomim.* **8**, 026003 (2013).
12. A. D. Marchese, C. D. Onal, D. Rus, *Soft Robotics* **1**, 75–87 (2014).
13. R. Pfeifer, M. Lungarella, F. Iida, *Science* **318**, 1088–1093 (2007).
14. K. Suzumori, S. Iikura, H. Tanaka, *Control Syst. IEEE* **12**, 21–27 (1992).
15. Y.-L. Park *et al.*, *Bioinspir. Biomim.* **9**, 016007 (2014).
16. P. Polygerinos, Z. Wang, K. C. Galloway, R. J. Wood, C. J. Walsh, *Robot. Auton. Syst.*; available at www.sciencedirect.com/science/article/pii/S0921889014001729.
17. M. T. Tolley *et al.*, *Soft Robotics* **1**, 213–223 (2014).
18. H. Lipson, *Soft Robotics* **1**, 21–27 (2014).
19. K.-J. Cho *et al.*, *Int. J. Precision Eng. Manuf.* **10**, 171–181 (2009).
20. F. Ilievski, A. D. Mazzeo, R. F. Shepherd, X. Chen, G. M. Whitesides, *Angew. Chem.* **123**, 1930–1935 (2011).
21. E. Steltz, A. Mozeika, N. Rodenberg, E. Brown, H. M. Jaeger, in *Proceedings of the 2009 IEEE/RSJ International Conference on Intelligent Robots and Systems*, 10 to 15 October 2009, St. Louis, MO, pp. 5672–5677.
22. T. J. Roberts, E. Azizi, *J. Exp. Biol.* **214**, 353–361 (2011).
23. A. Miserez, T. Schneberk, C. Sun, F. W. Zok, J. H. Waite, *Science* **319**, 1816–1819 (2008).
24. Materials and methods are available as supplementary materials on *Science* Online.
25. R. F. Shepherd *et al.*, *Angew. Chem.* **125**, 2964–2968 (2013).
26. M. T. Tolley *et al.*, in *Proceedings of the 2014 IEEE/RSJ International Conference on Intelligent Robots and Systems*, 14 to 18 September 2014, Chicago, IL, pp. 561–566.
27. M. Loepfe, C. M. Schumacher, U. B. Lustenberger, W. J. Stark, *Soft Robotics* **2**, 33–41 (2015).

ACKNOWLEDGMENTS

This material is based on work supported by NSF under award number DMR-1420570; the Wyss Institute for Biologically Inspired Research; and an Army Research Office, National Defense Science and Engineering Graduate (NDSEG) fellowship. Any opinions, findings, conclusions, or recommendations expressed in this material are those of the authors and do not necessarily reflect those of the funding organizations.

SUPPLEMENTARY MATERIALS

www.sciencemag.org/content/349/6244/161/suppl/DC1
Materials and Methods
Supplementary Text
Figs. S1 and S2
Table S1
References (*28*, *29*)
Movies S1 and S2

27 February 2015; accepted 11 June 2015
10.1126/science.aab0129

APPLIED PHYSICS

Mid-infrared plasmonic biosensing with graphene

Daniel Rodrigo,[1] Odeta Limaj,[1] Davide Janner,[2] Dordaneh Etezadi,[1] F. Javier García de Abajo,[2,3] Valerio Pruneri,[2,3] Hatice Altug[1]*

Infrared spectroscopy is the technique of choice for chemical identification of biomolecules through their vibrational fingerprints. However, infrared light interacts poorly with nanometric-size molecules. We exploit the unique electro-optical properties of graphene to demonstrate a high-sensitivity tunable plasmonic biosensor for chemically specific label-free detection of protein monolayers. The plasmon resonance of nanostructured graphene is dynamically tuned to selectively probe the protein at different frequencies and extract its complex refractive index. Additionally, the extreme spatial light confinement in graphene—up to two orders of magnitude higher than in metals—produces an unprecedentedly high overlap with nanometric biomolecules, enabling superior sensitivity in the detection of their refractive index and vibrational fingerprints. The combination of tunable spectral selectivity and enhanced sensitivity of graphene opens exciting prospects for biosensing.

Graphene has the potential to reshape the landscape of photonics and optoelectronics owing to its exceptional optical and electrical properties (*1*–*3*). In particular, its infrared (IR) response is characterized by long-lived collective electron oscillations (plasmons) that can be dynamically tuned by electrostatic gating, in contrast to conventional plasmonic materials such as noble metals (*4*–*10*). Furthermore, the electromagnetic fields of graphene IR plasmons display unprecedented spatial confinement, making them extremely attractive for enhanced light-matter interactions and integrated mid-IR photonics (*11*–*14*). Specifically, biosensing is an area in which graphene tunability and IR light localization offer great opportunities.

The mid-IR range is particularly well suited for biosensing, as it encompasses the molecular vibrations that uniquely identify the biochemical building blocks of life, such as proteins, lipids, and DNA (*15*). IR absorption spectroscopy is a powerful technique that provides exquisite biochemical information in a nondestructive label-free fashion by accessing these vibrational fingerprints. Nevertheless, vibrational absorption signals are prohibitively weak because of the large mismatch between mid-IR wavelengths (2 to 6 μm) and biomolecular dimensions (<10 nm). To overcome this limitation, high sensitivity can be achieved by exploiting the strong optical near fields in the vicinity of resonant metallic nanostructures (*16*–*18*); however, this comes at the expense of a reduced spectral bandwidth and is ultimately limited by the relatively poor field confinement of metals in the mid-IR (*19*).

Here, we report a graphene-based tunable mid-IR biosensor and demonstrate its potential for quantitative protein detection and chemical-specific molecular identification. Our device (Fig. 1A) consists of a graphene layer synthesized by chemical vapor deposition and transferred to a 280-nm-thick native silica oxide of a silicon substrate. Graphene nanoribbon arrays (width W = 20 to 60 nm and period $P \approx 2W$) are then patterned using electron beam lithography and oxygen plasma etching (*20*). A scanning electron microscope image and an atomic force microscope profile for typical samples are shown in Fig. 1, B and C. We apply an electrostatic field across the SiO_2 layer through a bias voltage (V_g)

[1]Institute of BioEngineering, École Polytechnique Fédérale de Lausanne, CH-1015 Lausanne, Switzerland. [2]Institut de Ciències Fotòniques, Mediterranean Technology Park, 08860 Castelldefels (Barcelona), Spain. [3]Institució Catalana de Recerca i Estudis Avançats, 08010 Barcelona, Spain.
*Corresponding author. E-mail: hatice.altug@epfl.ch

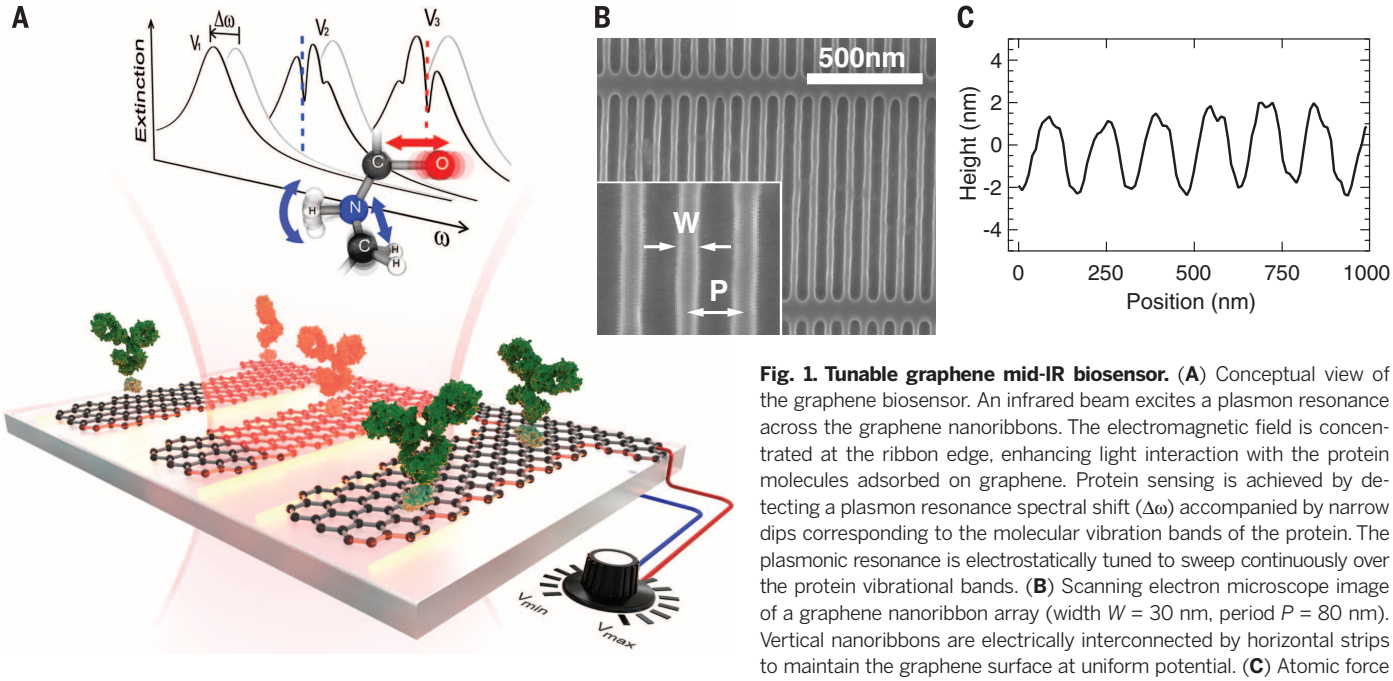

Fig. 1. Tunable graphene mid-IR biosensor. (**A**) Conceptual view of the graphene biosensor. An infrared beam excites a plasmon resonance across the graphene nanoribbons. The electromagnetic field is concentrated at the ribbon edge, enhancing light interaction with the protein molecules adsorbed on graphene. Protein sensing is achieved by detecting a plasmon resonance spectral shift (Δω) accompanied by narrow dips corresponding to the molecular vibration bands of the protein. The plasmonic resonance is electrostatically tuned to sweep continuously over the protein vibrational bands. (**B**) Scanning electron microscope image of a graphene nanoribbon array (width W = 30 nm, period P = 80 nm). Vertical nanoribbons are electrically interconnected by horizontal strips to maintain the graphene surface at uniform potential. (**C**) Atomic force microscope cross section of a graphene nanoribbon array.

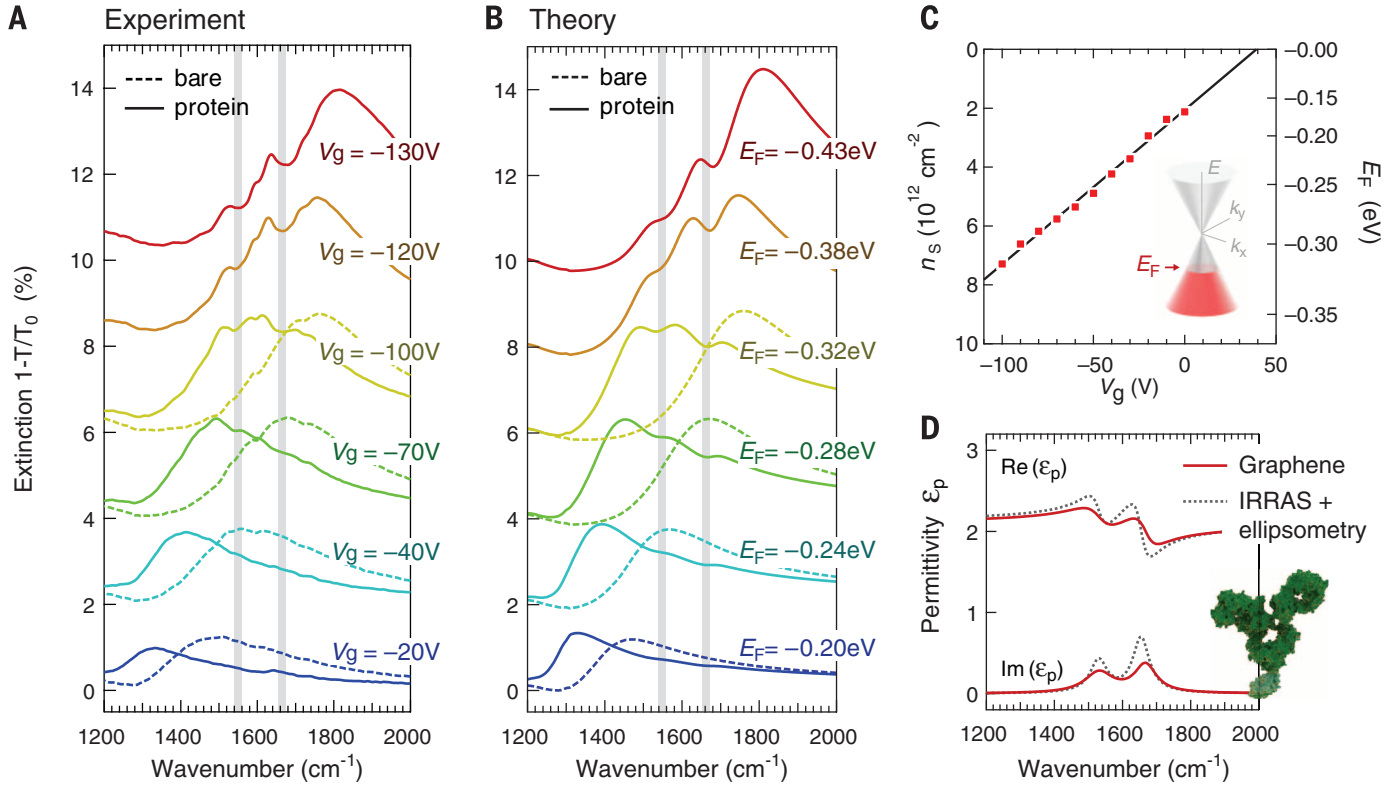

Fig. 2. Mid-IR spectrum of the graphene biosensor. (**A**) Extinction spectra of the graphene nanoribbon array (W = 30 nm, P = 80 nm) for bias voltages V_g from −20 V to −130 V before (dashed curves) and after (solid curves) protein bilayer formation. Extinction is calculated as the relative difference in transmission between regions with (T) and without (T_0) graphene nanoribbons. Gray vertical strips indicate amide I and II vibrational bands of the protein. (**B**) Analytic calculation of the extinction spectra after fitting graphene and protein parameters to reproduce experimental data. (**C**) Graphene carrier density (n_s) and Fermi energy (E_F) extracted from experimental IR extinction spectra of the bare graphene nanoribbon array at different applied bias voltages V_g. (**D**) Permittivity of the protein bilayer extracted from the analytic fit to the experimental IR spectra (solid red curves) of the graphene biosensor compared to the permittivity extracted from IRRAS and ellipsometry measurements (dashed black curves). Upper and lower curves show the real and imaginary components, respectively.

that is varied between 0 and 120 V to dynamically control the Fermi level (E_F) of graphene. Extinction spectra of the device are acquired using Fourier transform infrared (FTIR) spectroscopy for the incident electric field polarized perpendicular to the nanoribbons. Figure 2A shows the extinction for a nanoribbon array with W = 30 nm, P = 80 nm, and different values of V_g (dashed curves). A prominent resonance is observed, which is associated with localized surface plasmons (LSPs) polarized across the nanoribbons. By changing V_g, the resonance frequency is tuned continuously from 1450 cm^{-1} to above 1800 cm^{-1}. The ribbon width W = 30 nm is chosen so that the frequency tuning range sweeps across the target vibrational fingerprints (fig. S1).

We sought to detect protein molecules, the primary material of life enabling most of the critical biological functions. The main vibrational fingerprints of proteins are amide I and II bands (1660 and 1550 cm^{-1}), which are primarily associated with the C=O stretch and N-H bend modes in the amide functional group. For demonstration of protein detection, we used recombinant protein A/G and goat anti-mouse immunoglobulin G (IgG). Incubation of A/G on the sensor surface allows the formation of a protein monolayer by physisorption, which is then used to bind IgG antibodies and form a well-defined protein bilayer (*20*). The extinction spectra of the sensor are presented in Fig. 2A before and after protein bilayer formation, showing radical changes upon protein immobilization. The first observed prominent effect is a red shift of the plasmonic resonance as a consequence of the change in the refractive index at the sensor surface. Despite the nanometric thickness of the protein bilayer, we detected frequency shifts exceeding 200 cm^{-1}. The second prominent effect is the emergence of two spectral dips at 1660 cm^{-1} and 1550 cm^{-1} that are almost undetectable when they are far from the plasmonic resonance (e.g., for V_g = −20 V) and become progressively more intense with increasing spectral overlap (e.g., for V_g = −130 V). Their spectral positions coincide with the amide I and II bands, respectively, unambiguously revealing the presence of the protein compounds in a chemically specific manner. The decrease in extinction induced by the vibrational modes is the result of resonant coupling between plasmons and molecular vibrations (*21*).

To extract quantitative information on the protein optical parameters, we use an analytical model of the IR response of the graphene nanoribbon array (*22*). We model graphene in the electrostatic limit (W, P << λ) under the assumption that the ribbon response is dominated by the lowest-order transversal mode. The model involves a detailed account of the protein layer; however, a reasonable agreement is obtained in the limit of a thick protein layer. The transmission coefficient of the structure then reduces to

$$t = t_0 + \frac{i4\pi^2\alpha^{eff}(\omega)(1+r_0)t_0}{n_2 P\lambda} \quad (1)$$

where

$$\alpha^{eff}(\omega) = \frac{0.894W^2}{\frac{A}{n_1^2+n_2^2} - \frac{i\omega W}{\sigma(\omega)}} \quad (2)$$

is an effective graphene-ribbon polarizability that takes into account the complex refractive indices of the silica substrate n_2 (*23*) and the material immediately above the ribbons n_1, while the coefficient A is a function of P/W (in particular, A = 28.0 for P/W = 2.67). Here, t_0 and r_0 are the transmission and reflection coefficients of the interface between media 1 and 2 in the absence of graphene. The response of the latter enters through its frequency-dependent surface conductivity σ(ω), which we model in the local random-phase approximation (*11*). Finally, we compute the ratio of transmission in regions with and without graphene as $|t/t_0|^2$, which is the magnitude measured in the experiments.

We first used the analytic model to extract the graphene parameters from experimental IR spectra for bare nanoribbons (i.e., with n_1 = 1). The calculated spectra are reported in Fig. 2B (dashed curves) for the extracted relaxation time (τ = 15 fs) and

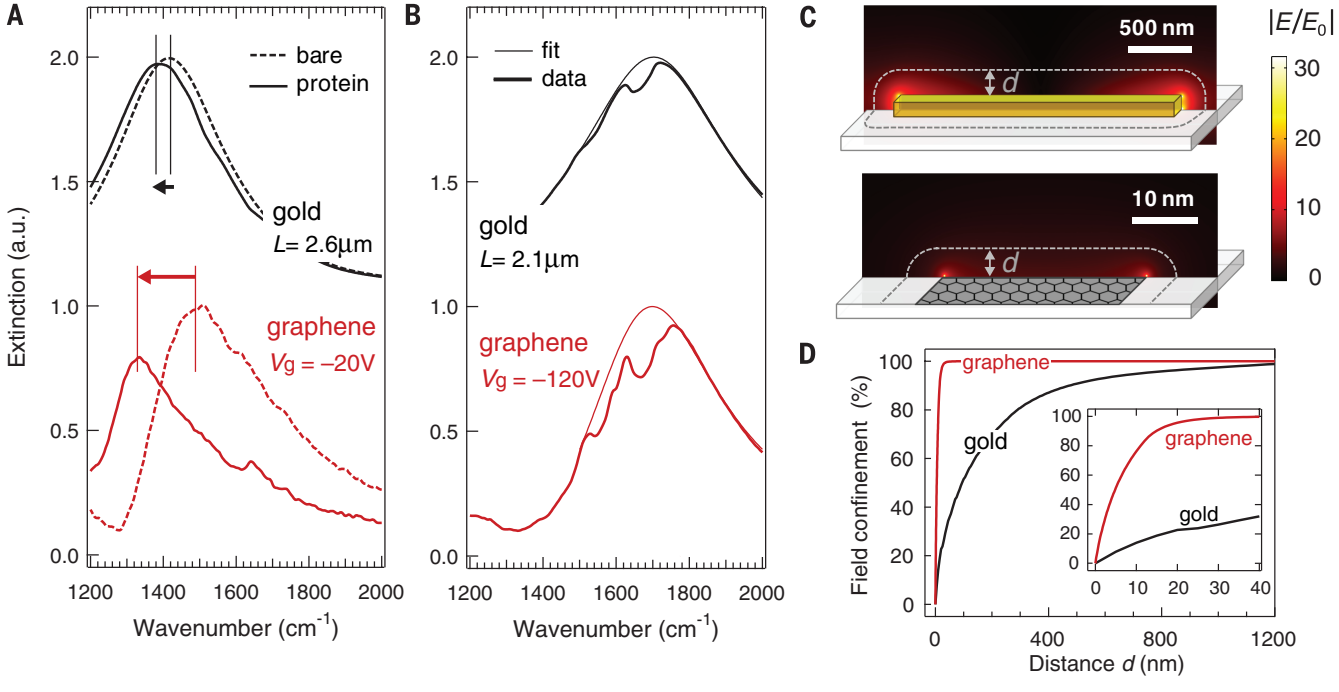

Fig. 3. Graphene versus gold. (**A**) Extinction spectra of graphene and gold nanoantenna arrays before (dashed curves) and after (solid curves) protein bilayer formation for plasmonic resonance peak away from the molecular vibration bands. The gold antennas have dimensions 2.6 µm × 0.2 µm × 0.1 µm while the graphene is biased to V_g = −20 V. The spectral shift of the plasmonic resonance (indicated by horizontal arrows) shows the refractive index sensitivity of the biosensors. (**B**) Extinction spectra of graphene and gold biosensors after protein formation (thick curves) and fitting (thin curves) for plasmon peak overlapping with the molecular vibration bands. The gold antennas have dimensions 2.1 µm × 0.2 µm × 0.1 µm and the graphene gate voltage is V_g = −120 V. The intensity of the spectral features at amide I and II bands (1660 to 1550 cm^{-1}) indicates the SEIRA sensitivity of the biosensors. (**C**) Near-field enhancement distribution $|E/E_0|$ in the plasmonic sensors operating at 1600 cm^{-1} resonance frequency. (**D**) Percentage of space-integrated near-field intensity confined within a volume extending a distance d outside the nanoantenna. Inset shows a zoom-in for d between 0 and 40 nm.

Fermi energies (E_F = −0.17 to −0.43 eV). We observe that the carrier density ($n_s \sim E_F^2$) changes linearly with V_g (Fig. 2C) and graphene has an intrinsic doping E_{F0} = −0.17 eV produced by charge transfer from the silica. Next, the analytic model is used to retrieve the protein permittivity from experimental results by adjusting a Lorentzian permittivity

$$\varepsilon_p(\omega) = n_1^2 = n_\infty^2 + \sum_{k=1}^{2} \frac{S_k^2}{\omega_k^2 - \omega^2 - i\omega\gamma_k} \quad (3)$$

Good agreement is observed between experimental and calculated spectra (Fig. 2B) for the protein Lorentzian parameters upon least-squares fitting. The extracted permittivity has a nondispersive term n_∞^2 = 2.08 and shows two absorption peaks at 1668 and 1532 cm^{-1}, matching the amide I and II bands, respectively (Fig. 2D). The fitted permittivity is also in good agreement with independent protein permittivity measurements from ellipsometry for n_∞^2 and IR reflection absorption spectroscopy (IRRAS) for S_k, ω_k, and γ_k (*20*). There is, however, a small discrepancy, which we attribute to a slight overestimate of plasmon-protein coupling in the theoretical model. These results indicate that the proposed graphene biosensor combines refractive index sensing, so far a prerogative of visible plasmonic sensors, with the unique chemical specificity of mid-IR spectroscopy, together with the extra degree of freedom enabled by the graphene electro-optical tunability.

The characteristics of our graphene biosensor become more evident by comparing its spectral response to that of a state-of-the-art metallic localized surface plasmon resonance (LSPR) sensor composed of a gold dipole-antenna array (Fig. 3). Both devices are first operated in a spectral range free of protein vibrational modes by setting graphene at V_g = −20 V and designing a gold dipole length L = 2.6 μm (Fig. 3A). Upon protein immobilization, we detect a resonance shift of 160 cm^{-1} for graphene, which is approximately 6 times the 27 cm^{-1} shift obtained with gold. Next, the operation spectrum is moved toward the protein amide I and II bands by setting graphene at V_g = −120 V and using a different gold sensor with L = 2.1 μm (Fig. 3B). Clearly, dynamic tunability of graphene is one of its main advantages over gold for surface-enhanced IR absorption (SEIRA), enabling sensing over a broad spectrum with a single device. In addition, for the SEIRA signal corresponding to the amide I band, the graphene sensor features a signal modulation of 27%, which is almost 3 times that observed with the gold sensor (11%).

The large spectral shifts and absorption signals confirm the unprecedented sensitivity of our graphene biosensor to the complex refractive index of the target molecule. For similar IR-frequency plasmons, the graphene atomic thickness leads to a higher confinement, resulting in a much larger spatial overlap between the mid-IR plasmonic field and the analyte. Figure 3C shows the near-field distribution of LSPR modes in graphene nanoribbons and gold dipole arrays calculated with a finite-element method. The field hotspots are located at the endpoints of the gold dipole and along the edges of the graphene nanoribbon. By computing the percentage of near-field intensity confined within a given distance d from the structure (Fig. 3D), we observe that 90% of the mode energy is confined within 15 nm from the graphene surface, whereas the same percentage is spread over a distance 500 nm away from the gold surface, thus confirming the tighter field confinement of graphene in the mid-IR. As the biosensing signal comes only from the field inside the target volume, we also calculate the field overlap with an 8-nm-thick protein bilayer, which is 29% for graphene versus only 4% for gold. The near-field intensity overlap can be experimentally extracted as the ratio of the relative resonance shift ($\Delta\omega/\omega$) and the permittivity variation ($\varepsilon_p - \varepsilon_{air}$) (*24*). This estimate yields 26% and 5% field overlap for graphene and gold, in good agreement with simulations (see above). These results demonstrate the ability of graphene to provide stronger light-protein interactions beyond state-of-the-art metallic plasmonic sensors; further improvement in the graphene quality should lead to even better sensitivity and spectral resolution.

REFERENCES AND NOTES

1. A. N. Grigorenko, M. Polini, K. S. Novoselov, *Nat. Photonics* **6**, 749–758 (2012).
2. F. J. García de Abajo, *Science* **339**, 917–918 (2013).
3. A. Vakil, N. Engheta, *Science* **332**, 1291–1294 (2011).
4. M. Jablan, H. Buljan, M. Soljacic, *Phys. Rev. B* **80**, 245435 (2009).
5. L. Ju *et al.*, *Nat. Nanotechnol.* **6**, 630–634 (2011).
6. H. Yan *et al.*, *Nat. Photonics* **7**, 394–399 (2013).
7. A. Woessner *et al.*, *Nat. Mater.* **14**, 421–425 (2015).
8. Z. Fang *et al.*, *ACS Nano* **7**, 2388–2395 (2013).
9. V. W. Brar *et al.*, *Nano Lett.* **13**, 2541–2547 (2013).
10. Z. Fei *et al.*, *Nature* **487**, 82–85 (2012).
11. F. H. L. Koppens *et al.*, *Nano Lett.* **11**, 3370–3377 (2011).
12. B. Vasić *et al. J. Appl. Phys.* **113**, 013110 (2013).
13. Y. Li *et al.*, *Nano Lett.* **14**, 1573–1577 (2014).
14. P. Li *et al.*, *Nano Lett.* **14**, 4400–4405 (2014).
15. P. R. Griffiths, J. A. De Haseth, *Fourier Transform Infrared Spectrometry* (Wiley, New York, 2007).
16. F. Neubrech *et al.*, *Phys. Rev. Lett.* **101**, 157403 (2008).
17. R. Adato, H. Altug, *Nat. Commun.* **4**, 2154 (2013).
18. C. Wu *et al.*, *Nat. Mater.* **11**, 69–75 (2012).
19. Y. Zhong *et al.*, *J. Nanophotonics* **9**, 093791 (2015).
20. See supplementary materials on *Science* Online.
21. R. Adato *et al.*, *Nano Lett.* **13**, 2584–2591 (2013).
22. F. J. García de Abajo, *ACS Photonics* **1**, 135–152 (2014).
23. E. D. Palik, *Handbook of Optical Constants of Solids* (Academic Press, New York, 1998).
24. J. D. Joannopoulos *et al.*, *Photonic Crystals: Molding the Flow of Light* (Princeton Univ. Press, Princeton, NJ, 2011).

ACKNOWLEDGMENTS

Supported by European Commission grants FP7-IEF-2013-625673-GRYPHON, Graphene Flagship CNECT-ICT-604391, and FP7-ICT-2013-613024-GRASP; the Spanish Ministry of Economy and Competitiveness (MINECO) "Fondo Europeo de Desarrollo Regional" (FEDER) through grant TEC2013-46168-R; NATO's Public Diplomacy Division in the framework of "Science for Peace"; European Union's Horizon 2020 research and innovation program under grant agreement No 644956; the Swiss National Science Foundation through project 133583; and Fundació Privada Cellex, the Severo Ochoa Program, and the Ramon y Cajal fellowship program. We also acknowledge École Polytechnique Fédérale de Lausanne and Center of MicroNano Technology for financial support and nanofabrication. This paper is dedicated to the memory of our friend and colleague, Julien Perruisseau-Carrier.

SUPPLEMENTARY MATERIALS

www.sciencemag.org/content/349/6244/165/suppl/DC1
Materials and Methods
Supplementary Text
Figs. S1 to S3
Reference (*25*, *26*)

11 April 2015; accepted 4 June 2015
10.1126/science.aab2051

GALAXY EVOLUTION

An over-massive black hole in a typical star-forming galaxy, 2 billion years after the Big Bang

Benny Trakhtenbrot,[1]* C. Megan Urry,[2,3,4] Francesca Civano,[3,5] David J. Rosario,[6] Martin Elvis,[5] Kevin Schawinski,[1] Hyewon Suh,[5,7] Angela Bongiorno,[8] Brooke D. Simmons[9]

Supermassive black holes (SMBHs) and their host galaxies are generally thought to coevolve, so that the SMBH achieves up to about 0.2 to 0.5% of the host galaxy mass in the present day. The radiation emitted from the growing SMBH is expected to affect star formation throughout the host galaxy. The relevance of this scenario at early cosmic epochs is not yet established. We present spectroscopic observations of a galaxy at redshift z = 3.328, which hosts an actively accreting, extremely massive BH, in its final stages of growth. The SMBH mass is roughly one-tenth the mass of the entire host galaxy, suggesting that it has grown much more efficiently than the host, contrary to models of synchronized coevolution. The host galaxy is forming stars at an intense rate, despite the presence of a SMBH-driven gas outflow.

Several lines of observational evidence, spanning a wide range of cosmic epochs, have led to a commonly accepted picture wherein supermassive black holes (SMBHs, $M_{BH} > 10^6\,M_\odot$; $M_\odot$ is the solar mass) coevolve with their host galaxies (*1*–*4*). Moreover, energy- and/or momentum-driven "feedback" from accreting SMBHs (Active Galactic Nuclei; AGN) is thought to quench star formation in the host galaxy (*5*). To directly test the relevance of such scenarios at